Article

Spectroscopic and Kinetic Studies of *Arabidopsis thaliana* Sulfite Oxidase: Nature of the Redox-Active Orbital and Electronic Structure Contributions to Catalysis

Craig Hemann, Brian L. Hood, Meita Fulton, Robert Hnsch, Gnter Schwarz, Ralf R. Mendel, Martin L. Kirk, and Russ Hille

J. Am. Chem. Soc., **2005**, 127 (47), 16567-16577• DOI: 10.1021/ja0530873 • Publication Date (Web): 08 November 2005

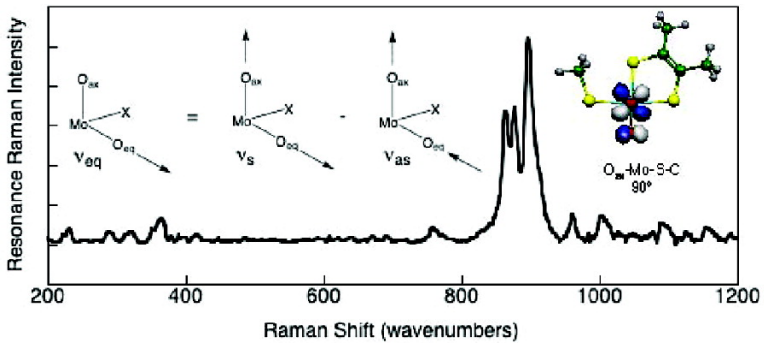

More About This Article

Additional resources and features associated with this article are available within the HTML version:

- Supporting Information
- Links to the 1 articles that cite this article, as of the time of this article download
- Access to high resolution figures
- Links to articles and content related to this article
- Copyright permission to reproduce figures and/or text from this article

View the Full Text HTML

J|A|C|S
ARTICLES
Published on Web 11/08/2005

Spectroscopic and Kinetic Studies of *Arabidopsis thaliana* Sulfite Oxidase: Nature of the Redox-Active Orbital and Electronic Structure Contributions to Catalysis

Craig Hemann,[†] Brian L. Hood,[†,¶] Meita Fulton,[‡] Robert Hänsch,[§] Günter Schwarz,[§] Ralf R. Mendel,[§] Martin L. Kirk,*[,‡] and Russ Hille*[,†]

Contribution from the Department of Molecular and Cellular Biochemistry, The Ohio State University, Columbus, Ohio 43210, Department of Chemistry, The University of New Mexico, MSC03 2060, 1 University of New Mexico, Albuquerque, New Mexico 87131-0001, and Department of Plant Biology, Technical University of Braunschweig, 38023 Braunschweig, Germany

Received May 11, 2005; E-mail: hille.1@osu.edu; mkirk@unm.edu

Abstract: Plant sulfite oxidase from *Arabidopsis thaliana* has been characterized both spectroscopically and kinetically. The enzyme is unusual in lacking the heme domain that is present in the otherwise highly homologous enzyme from vertebrate sources. In steady-state assays, the enzyme exhibits a pH maximum of 8.5 and is also found to function as a selenite oxidase. Sulfite at the lowest experimentally feasible concentrations reduces the enzyme within the dead-time of a stopped-flow instrument at 5 °C, indicating that the *A. thaliana* enzyme has a limiting rate constant for reduction, k_{red}, at least 10 times greater than that of the chicken enzyme (190 s^{-1}). The EPR parameters for the high- and low-pH forms of the *A. thaliana* enzyme have been determined, and the *g*-values are found to resemble those previously reported for the vertebrate enzymes. Finally, the *A. thaliana* enzyme has been probed by resonance Raman spectroscopy. A detailed analysis of the vibrational spectrum in the region where Mo═O stretching modes are anticipated to occur has been performed with the help of density functional theory calculations, evaluated in the context of the Raman data. Calculated frequencies obtained for two model systems have been compared to experimental resonance Raman spectra of oxidized *A. thaliana* sulfite oxidase catalytically cycled in both $H_2{}^{16}O$ and $H_2{}^{18}O$. The vibrational frequency shifts observed upon ^{18}O-labeling of the enzyme are consistent with theoretical models in which either the equatorial oxygen or both equatorial and axial atoms of the dioxomolybdenum center are labeled. Importantly, the vibrational mode description is consistent with the active site possessing geometrically inequivalent oxo ligands and a Mo d_{xy} redox-active molecular orbital oriented in the equatorial plane forming a π-bonding interaction solely with the equatorial oxo, O_{eq}. Electron occupancy of this Mo═O_{eq} π^* redox orbital upon interaction with substrates would effectively labilize the Mo═O_{eq} bond, providing the dominant contribution to lowering the activation energy for oxygen atom transfer.

Introduction

Sulfite oxidase (SO) catalyzes the oxidation of sulfite to sulfate, the final step in the oxidative degradation of the sulfur containing amino acids and lipids (the latter being prevalent in the cell membranes of the myelin sheath). Deficiencies in this enzyme lead to severe neurological abnormalities and ultimately early death.[1] In vertebrates, the severe neurological disorders manifested by individuals with mutations in the structural gene for SO suggest that clinical symptoms arise principally from a dysfunction in lipid rather than protein metabolism.[2] SO belongs to a family of mononuclear molybdenum enzymes that includes the plant assimilatory nitrate reductases. These are enzymes whose oxidized active sites can be formulated as $LMo^{VI}O_2$(S-Cys),[3] with L representing a bidentate enedithiolate ligand[4] contributed by a pterin cofactor common to all mononuclear molybdenum and tungsten enzymes. There is general consensus that the coordination geometry of the metal center is distorted square-pyramidal, with one of the two terminal oxo ligands occupying the axial position, and the remaining one in the equatorial plane *trans* to a dithiolate sulfur donor (Scheme 1).

Sulfite oxidases from mammalian and avian sources have been studied by a variety of spectroscopic methods, including magnetic circular dichroism (MCD),[3,8] continuous-wave electron paramagnetic resonance (CW-EPR),[5−8] pulsed EPR techniques,

[†] The Ohio State University.
[‡] The University of New Mexico.
[§] Technical University of Braunschweig.
[¶] Present address: Laboratory of Proteomics and Analytical Technologies, Research Technology Group, SAIC-Frederick, Inc., National Cancer Institute at Frederick, 1050 Boyle St., Ft. Detrick, Frederick, Maryland 21702.

(1) (a) Johnson, J. L.; Waud, W. R.; Rajagopalan, K. V.; Duran, M.; Beemer, F. A.; Wadman, S. K. *Proc. Natl. Acad. Sci. U.S.A.* **1980**, *77*, 3715−3719. (b) Rajagopalan, K. V.; Johnson, J. L. *J. Biol. Chem.* **1992**, *267*, 10199−10202.
(2) Johnson, J. L.; Wadman, S. K. In *Metabolic Basis of Inherited Disease*, 6th ed.; Scriver, C. R., Bandet, A. L., Sly, W. S., Valle, D., Eds.; McGraw-Hill: New York, 1989; Vol. 1, pp 1463−1475.
(3) Hille, R. *Chem. Rev.* **1996**, *96*, 2757−2816.
(4) Kirk, M. L.; McNaughton, R. L.; Helton, M. E. *Prog. Inorg. Chem.* **2004**, *52*, 111−212.

Scheme 1. Catalytic Cycle of SO

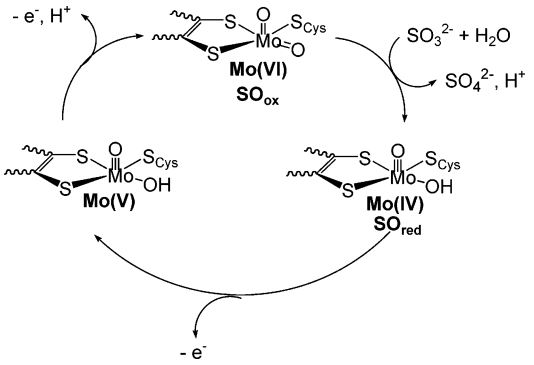

electron spin−echo−envelope modulation (ESEEM), hyperfine sublevel correlation spectroscopy (HYSCORE),[47] and electron nuclear double resonance (ENDOR),[9−11] extended X-ray absorption fine spectra (EXAFS),[12,13] and resonance Raman spectroscopy.[14,15] In addition, the X-ray crystal structure of the reduced form of the enzyme from chicken liver has been reported at a resolution of 1.9 Å.[16] The enzyme is a homodimer (typically 110 kDa) containing an N-terminal cytochrome b_5-type domain, a central molybdenum-binding domain, and a C-terminal dimerization domain. The active site is positioned at the bottom of a positively charged binding pocket, with a molybdenum coordinated hydroxyl ligand, presumably derived from O_{eq} in the oxidized enzyme, facing into the solvent access channel.

Atypical sulfite oxidases have been found which do not have the same redox-active centers as the mammalian and avian enzymes. For example, sulfite:cytochrome *c* oxidoreductase from *Starkya novella* is a heterodimeric enzyme, possessing a 40.6 kDa molybdenum-containing protein and an associated 8.8 kDa cytochrome c_{552} protein rather than a *b*-type cytochrome.[37,45,46] Reduction of sulfite results in transfer of electrons from the molybdenum to the cytochrome c_{552} and further on to another cytochrome *c*. Recently, a SO from *Arabidopsis thaliana* has been cloned, expressed, and initially characterized, including determination of its crystal structure.[18,36] This plant enzyme is a 43.3 kDa monomeric protein containing only the molybdenum center and is devoid of other redox-active cofactors and chromophores. While the enzyme does not contain a heme domain, it has been suggested that a *b*-type cytochrome would be its physiological electron acceptor. The lack of an associated heme domain makes it unique to eukaryotic sulfite oxidases and provides an ideal situation for using resonance Raman spectroscopy to probe the vibrational and electronic structure of the molybdenum center without complications from other chromophores or the need for additional steps in enzyme preparation, such as tryptic cleavage, to remove a heme domain. Here we report a resonance Raman spectroscopic investigation of oxidized plant SO with a specific emphasis on understanding the high-frequency Mo═O stretching region for enzyme cycled in both $H_2{}^{16}O$ and $H_2{}^{18}O$. The vibrational frequency differences among the various isotopomers have been interpreted using the results of density functional calculations performed on two different models of the molybdenum center of SO. Our analysis of the Raman spectra of oxidized *A. thaliana* SO provides the basis for understanding electronic and geometric structure/activity relationships related to catalysis in this and related mononuclear molybdenum enzymes.

Experimental Section

Protein Expression and Purification. SO from *A. thaliana* was expressed and purified according to Eilers et al.[18] with the following

(5) Lamy, M. T.; Gutteridge, S.; Bray, R. C. *Biochem. J.* **1980**, *185*, 397−403.
(6) Bray, R. C.; Gutteridge, S.; Lamy, M. T.; Wilkinson, T. *Biochem. J.* **1983**, *211*, 227−236.
(7) Dhawan, I. K.; Enemark, J. H. *Inorg. Chem.* **1996**, *35*, 4873−4882.
(8) Cramer, S. P.; Johnson, J. L.; Rajagopalan, K. V.; Sorrell, T. N. *Biochem. Biophys. Res. Commun.* **1979**, *91*, 434−439.
(9) Pacheco, A.; Basu, P.; Borbat, P.; Raitsimring, A. M.; Enemark, J. H. *Inorg. Chem.* **1996**, *35*, 7001−7008.
(10) Raitsimring, A. M.; Pacheco, A.; Enemark, J. H. *J. Am. Chem. Soc.* **1998**, *120*, 11263−11278.
(11) (a) Astashkin, A. V.; Mader, M. L.; Pacheco, A.; Enemark, J. H.; Raitsimring, A. M. *J. Am. Chem. Soc.* **2000**, *122*, 5294−5302. (b) Astashkin, A. V.; Raitsimring, A. M.; Feng, C.; Johnson, J. L.; Rajagopalan, K. V.; Enemark, J. H. *J. Am. Chem. Soc.* **2002**, *124*, 6109−6118.
(12) Cramer, S. P.; Wahl, R.; Rajagopalan, K. V. *J. Am. Chem. Soc.* **1981**, *103*, 7721−7727.
(13) George, G. N.; Kipke, C. A.; Prince, R. C.; Sunde, R. A.; Enemark, J. H.; Cramer, S. C. *Biochemistry* **1989**, *28*, 5075−5080.
(14) Garton, S. D.; Garrett, R. M.; Rajagopalan, K. V.; Johnson, M. K. *J. Am. Chem. Soc.* **1997**, *119*, 2590−2591.
(15) Johnson, M. K.; Garton, S. D.; Oku, H. *J. Biol. Inorg. Chem.* **1997**, *2*, 797−803.
(16) Kisker, C.; Schindelin, H.; Pacheco, A.; Wehbi, W. A.; Garrett, R. M.; Rajagopalan, K. V.; Enemark, J. H.; Rees, D. C. *Cell* **1997**, *91*, 973−983.
(17) Gardlik, S.; Rajagopalan, K. V. *J. Biol. Chem.* **1991**, *266*, 4889−4895.
(18) Eilers, T.; Schwarz, G.; Brinkmann, H.; Witt, C.; Richter, T.; Nieder, J.; Koch, B.; Hille, R.; Hänsch, R.; Mendel, R. R. *J. Biol. Chem.* **2001**, *276*, 46989−46994.
(19) (a) Frisch, M. J. et al. *Gaussian 98*, revision A11.3; Gaussian, Inc.: Pittsburgh, PA, 2002. (b) Frisch, M. J. et al. *Gaussian 03*, revision C.02; Gaussian, Inc.: Wallingford CT, 2004.
(20) Becke, A. D. *J. Chem. Phys.* **1993**, *98*, 5648.
(21) Becke, A. D. *Phys. Rev.* **1988**, *A38*, 3098.
(22) Lee, C.; Yang, W.; Parr, R. G. *Phys. Rev.* **1988**, *37B*, 785.
(23) Hehre, W. J.; Radom, L.; Schleyer, P. v. R.; Pople, J. A. *Ab initio Molecular Orbital Theory*; Wiley: New York, 1985; Chapter 4.
(24) (a) Hay, P. J.; Wadt, W. R. *J. Chem. Phys.* **1985**, *82*, 270. (b) Wadt, W. R.; Hay, P. J. *J. Chem. Phys.* **1985**, *82*, 284. (c) Hay, P. J.; Wadt, W. R. *J. Chem. Phys.* **1985**, *82*, 299.
(25) Brody, M. S.; Hille, R. *Biochemistry* **1999**, *38*, 6668−6677.
(26) Rivera, M.; Barillas-Mury, C.; Christiansen, K. A.; Little, J. W.; Wells, M. A.; Walker, F. A. *Biochemistry* **1992**, *31*, 12233−12240.
(27) McCord, J. M.; Fridovich, I. *J. Biol. Chem.* **1968**, *243*, 5753−5760.
(28) Fridovich, I. *J. Biol. Chem.* **1970**, *245*, 4053−4057.
(29) Johnson, J. L.; Rajagopalan, K. V. *J. Biol. Chem.* **1977**, *252*, 2017−2025.
(30) Garrett, R. M.; Rajagopalan, K. V. *J. Biol. Chem.* **1996**, *271*, 7387−7391.
(31) Temple, C. A.; Graf, T. N.; Rajagopalan, K. V. *Arch. Biochem. Biophys.* **2000**, *383*, 281−287.
(32) (a) Cohen, H. J.; Fridovich, I. *J. Biol. Chem.* **1971**, *246*, 359−366. (b) Cohen, H. J.; Fridovich, I. *J. Biol. Chem.* **1971**, *246*, 367−373. (c) Cohen, H. J.; Fridovich, I.; Rajagopalan, K. V. *J. Biol. Chem.* **1971**, *246*, 374−382.
(33) Kessler, D. L.; Rajagopalan, K. V. *J. Biol. Chem.* **1972**, *247*, 6566−6573.
(34) (a) Willis, L. J.; Loehr, T. M. *Spectrochim. Acta* **1987**, *13A*, 51−58. (b) Johnson, M. K. *Prog. Inorg. Chem.* **2004**, *52*, 213−266.
(35) Peariso, K.; McNaughton, R. L.; Kirk, M. L. *J. Am. Chem. Soc.* **2002**, *124*, 9006.
(36) Schrader, N.; Fischer, K.; Theis, K.; Mendel, R. R.; Schwarz, G.; Kisker, C. *Structure* **2003**, *11*, 1251−1263.
(37) Kappler, U.; Bennett, B.; Rethmeier, J.; Schwarz, G.; Deutzmann, R.; McEwan, A. G.; Dahl, C. *J. Biol. Chem.* **2000**, *275*, 13202−13212.
(38) Helton, M. E.; Pacheco, A.; McMaster, J.; Enemark, J. H.; Kirk, M. L. *J. Inorg. Biochem.* **2000**, *80*, 227−233.
(39) Albrecht, A. C. *J. Chem. Phys.* **1961**, *34*, 1471.
(40) (a) Johnson, M. K. *Prog. Inorg. Chem.* **2004**, *52*, 213−266. (b) Willis, L. J.; Loehr, T. M.; Miller, K. F.; Bruce, A. E.; Stiefel, E. I. *Inorg. Chem.* **1986**, *25*, 4289−4293. (c) Oku, H.; Ueyama, N.; Nakamura, A. *Inorg. Chem.* **1995**, *34*, 3667−3676.
(41) Hertzberg, G. *Infrared and Raman Spectra of Polyatomic Molecules*; Van Nostrand: New York, 1945.
(42) Izumi, Y.; Glaser, T.; Rose, K.; McMaster, J.; Basu, P.; Enemark, J. H.; Hedman, B.; Hodgson, K. O.; Solomon, E. I. *J. Am. Chem. Soc.* **1999**, *121*, 10035−10046.
(43) Flükiger, P.; Lüthi, H. P.; Portmann, S.; Weber, J. *Molekel 4.0*; Swiss Center for Scientific Computing: Manno,Switzerland, 2000.
(44) ChemCraft V1.4 beta (build 237) at http://www.chemcraftprog.com.
(45) Kappler, U.; McEwan, A. G. *FEBS Lett.* **2002**, *529*, 208.
(46) McEwan, A. G.; Kappler, U.; McDevitt, C. A. In *Microbial Molybdenum-Containing Enzymes in Respiration: Structural and Functional Aspects (Advances in Photosynthesis and Respiration)*; Zannoni, Ed. D., Ed.; Kluwer Academic Publishers: Dordrecht, The Netherlands, 2004; p 175.
(47) Astashkin, A. V.; Feng, C.; Raitsimring, A. M.; Enemark, J. H. *J. Am. Chem. Soc.* **2005**, *127*, 502−503.

modifications. TP1000 (ΔmoaAB) cells carrying the plasmid pQE-80-*sox* were grown aerobically at 30 °C for 24 h after induction with 0.1 mM isopropyl-β-thiogalactoside at low cell density ($A_{600} = 0.05$). Crude lysate from cell lysis/sonication was loaded onto a Ni−NTA column pre-equilibrated with lysis buffer (50 mM NaH_2PO_4, pH 8.0, 300 mM NaCl, 10 mM imidazole). The column was washed with 2−3 times the bed volume of lysis buffer followed by wash buffer consisting of 50 mM NaH_2PO_4, pH 8.0, 300 mM NaCl, 20 mM imidazole, until the eluate had an OD_{280} less than 0.05. SO was eluted with 100 mM imidazole lysis buffer. Fractions containing SO as judged by SDS−PAGE analysis were pooled, concentrated by ultrafiltration, and loaded onto a Mono-Q column pre-equilibrated with 50 mM NaH_2PO_4, pH 8.0. SO was eluted with the same buffer, and fractions were concentrated based on purity (UV−visible spectrum, SDS−PAGE). Concentrated SO was exchanged into 20 mM Tris-acetate, pH 8.0, 300 mM NaCl by gel filtration on a Sephadex G-25 column and stored at 5 °C for immediate use or in liquid nitrogen for long-term storage. Enzyme concentration was determined spectrophotometrically using an extinction coefficient of 69 820 M^{-1} cm^{-1} at 280 nm.[18]

SO Assays. Assays for SO were carried out in 20 mM Tris-acetate, pH 8.0 following reduction of potassium ferricyanide ($\epsilon = 1020$ M^{-1} cm^{-1}) at 420 nm[17] or reduction of cytochrome *c* ($\epsilon = 19\,630$ M^{-1} cm^{-1}) at 550 nm.[18] Steady-state kinetic measurements were performed aerobically at 25 °C using a 1.0 cm light path cuvette and a final sample buffer volume of 1.0 mL, monitoring reduction of ferricyanide. All buffers (in their conjugate base forms) were used at a concentration of 20 mM and adjusted to a pH of 8.0 with acetic acid to avoid the inclusion of inhibitory anions. The buffers used for the pH dependence profile were bis-Tris (pH 6.0−6.5), bis-Tris-propane (pH 7.0−7.5), Tris (pH 7.5−8.5), and glycine (pH 9.0−10.0). Sulfite concentration was varied from 5 to 200 μM, while ferricyanide was kept at a saturating concentration of 400 μM. Horse heart cytochrome *c* and superoxide dismutase solutions were purchased from Sigma and prepared in the appropriate buffer prior to use in the steady-state assays.

Rapid reaction kinetics were performed on an Applied Photophysics Inc. SX.18MV stopped-flow apparatus. Single-wavelength kinetic transients were measured at 360 nm using a photomultiplier tube and full spectrum analysis (250−750 nm) using a diode array detector. Reductive half-reactions were carried out anaerobically at 5 °C using varying concentrations of SO (7.5−25 μM) and sulfite (180−800 μM). Samples were made anaerobic by alternately flushing with argon and evacuating with vacuum every 10 min over the course of 1.5 h in a glass tonometer.

Spectroscopic Methods. UV−visible spectra and kinetic assays were recorded using a Hewlett-Packard 8452A single beam diode-array spectrophotometer. Reduction of the enzyme was performed using either sodium dithionite or sodium sulfite. Circular dichroism spectra were recorded using an AVIV Associates Model 40DS UV/VIS/NIR circular dichroism spectrometer.

Electron paramagnetic resonance spectra were recorded using a Brüker ER 300 spectrometer equipped with an ER 035 M gaussmeter and a Hewlett-Packard 5352 B microwave frequency counter. Temperature was controlled at 150 K using a Brüker ER 4111 VT continuous flow liquid nitrogen cryostat. Samples were prepared by exchange into the appropriate buffer through gel filtration. Sodium sulfite was added in a stoichiometric excess to the sample in an EPR tube, which had been flushed with argon for 15 min. A half-molar equivalent of ferricyanide solution was added to partially reoxidize the sample, which was then immediately frozen in a dry ice/acetone bath and stored in liquid nitrogen.

Resonance Raman spectra were recorded using 488 nm excitation from a Coherent Innova 307 argon ion laser. Plasma emission lines were removed using Pellin-Broca prisms and Rayleigh-scattered photons rejected using a holographic notch filter. Raman-scattered light was collected and dispersed using a single-stage spectrograph employing a Princeton Instruments 1024 KTB, back-thinned, charge-coupled device detector. Band positions were calibrated using an external indene standard and are accurate to ± 2 cm^{-1}. Data were collected from the surface of a 30 μL sample maintained at 30 K using a custom-built coldfinger and an APD Cryogenics closed-cycle helium refrigerator. Each sample was illuminated for several hours prior to data collection to reduce background fluorescence. Samples for resonance Raman studies were prepared in 50 mM Tricine buffer, pH 8.0, and were concentrated to 1−3 mM by Centricon ultrafiltration. Redox-cycled enzyme was prepared by reduction/reoxidation of the enzyme with an excess of sodium sulfite and ferricyanide, followed by gel-filtration. Exchange into $H_2{}^{18}O$ (95−97% isotopically enriched $H_2{}^{18}O$ from Isotec, Inc.) was accomplished by two 10-fold dilution/reconcentration cycles, reduction using sodium sulfite, and air reoxidation, followed by three additional 10-fold dilution/reconcentration cycles.

Computational Procedures. Vibrational modes for ^{16}O- and ^{18}O-substituted enzyme models were calculated using either the Gaussian 98W or Gaussian 03W software package.[19] All small model calculations employed the B3LYP hybrid functional using a spin-restricted formalism for the oxidized $[MoO_2(C_2S_2Me_2)(SMe)]^{1-}$ (Me = methyl) active site.[20−22] A 6-31G basis set was used for all nonmetal atoms, and a polarization function was added to the oxygen and sulfur atoms (6-31G*).[23] The LANL2DZ basis set and LANL2 effective core potentials were used for molybdenum.[24] Computational models substituting H_3-CS for the cysteine thiolate and $(CH_3)_2C_2S_2{}^2$ for the ene-1,2-dithiolate ligands were used. Bond lengths, bond angles, and dihedral angles for the computational model were obtained from full geometry optimization calculations. Additional calculations were performed with the O_{ax}−Mo−S−C(H_3) dihedral angle constrained to 90°, in accordance with the ∼90° O_{ax}−Mo−$S_{cysteine}$−C dihedral observed in the X-ray structure of the chicken enzyme. A large model was also investigated which included the full pyranopterin−dithiolene (dt) truncated at the phosphate side chain by a vinyl group. The 6-31G basis set was used for carbon and hydrogen atoms, the 6-31G** basis set was used for sulfur, nitrogen, and oxygen atoms, and the LANL2DZ basis set and LANL2 effective core potentials were used for molybdenum. As with the small model calculations, geometry optimizations were calculated for both an unconstrained model and for a model in which the O_{ax}−Mo−S−C(H_3) dihedral angle was fixed at 90°.

Results

Kinetics of Plant SO. To explore the effect of pH on the kinetics of SO, a steady-state analysis was carried out by varying the sulfite concentration from 5 to 200 μM while keeping ferricyanide constant at 400 μM over the pH range of 6.0−10.0. A plot of k_{cat} versus pH yields a bell-shaped curve, indicating a maximal activity at pH 8.5 and apparent pK_a values of 8.1 and 8.9 (Figure 1). A similar pH optimum was observed for k_{cat} versus pH for chicken SO, but that system had different pK_a values (7.0 and 10.2, respectively) than those seen for *A. thaliana* SO.[25]

A. thaliana SO lacks the cytochrome b_5 domain typical of mammalian and avian sulfite oxidases, and at present, the physiological electron acceptor is unknown. However, it has been suggested that a *b*-type cytochrome from plant peroxisomes is a likely candidate to fill this role.[18] We investigated the reactivity of SO with rat outer-mitochondrial membrane cytochrome b_5, which has extensive sequence homology with the heme domain of vertebrate sulfite oxidases,[26] and no reduction of the heme group was observed when SO was reacted with an excess of sulfite. Additional reactions were carried out using horse heart cytochrome *c* as electron acceptor. Reaction of SO with sulfite in the presence of cytochrome *c* showed a significantly slower activity than that observed with ferricyanide (∼1%). Addition of superoxide dismutase to the reaction mixture

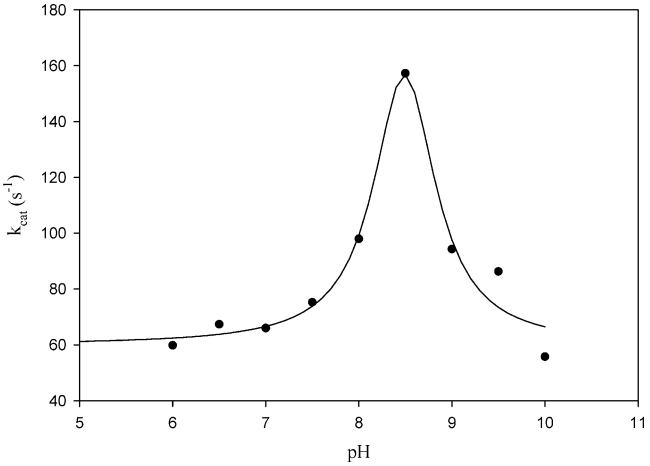

Figure 1. The pH dependence of *A. thaliana* SO. Experiments were performed as described in Materials and Methods. A pH optimum of 8.5 and apparent pK_a values of 8.1 and 8.9 are observed.

reduced the observed activity by almost half, suggesting that $O_2^{\bullet-}$ is mostly responsible for the observed reduction of cytochrome *c* and not due to electron transfer from SO.[27,28] Reaction of SO with selenite (SeO_3^{2-}) showed approximately 5% of the observed sulfite activity using ferricyanide as electron acceptor.

An extensive rapid kinetics study of the reaction of SO with sulfite was prohibited by the extremely rapid rate of the reaction. Single-wavelength transients showed that the reduction of the molybdenum center, even at the lowest concentrations of sulfite, was essentially complete within 5 ms after mixing at 5 °C in the stopped-flow apparatus. With a diode array detector, it was clear that reduction had already been completed after the first spectrum when compared with that of unreacted oxidized enzyme shot against buffer rather than a solution of sulfite. Longer reaction times did not show any appreciable reoxidation artifacts, ruling out the presence of oxygen in the tonometer (SO is observed to reoxidize relatively quickly with oxygen).

Spectroscopic Characterization of *A. thaliana* SO. With the addition of the Mono-Q chromatography step to the SO purification, which removed the apo-enzyme lacking the molybdenum center, an improved UV−visible absorption spectrum has been obtained over that reported previously (Figure 2A). The absorbance maxima at 360 and 480 nm correlate well with the maxima seen for the molybdenum domain cleavage products from native rat[29] and recombinant human[31] SO as well as a truncated expression construct of human SO.[31] The absorption maximum observed at 360 nm, which has been attributed to a dithiolene-to-molybdenum charge transfer transition(s), and the broad shoulder observed at 480 nm, proposed to arise from cysteine-to-molybdenum charge transfer, are readily evident. Upon reduction of the enzyme with either sulfite or dithionite, there is a loss of these observed maxima with a slight increase in absorption intensity appearing at approximately 400 nm, again consistent with previous results with enzyme from vertebrate sources. A circular dichroism spectrum of SO shows strong positive features at approximately 370 and 485 nm (Figure 2B). No additional features were observed out to 1200 nm for the oxidized enzyme.

It is well-established that vertebrate sulfite oxidases yield different Mo(V) EPR spectra depending on experimental conditions (e.g., pH and anion concentration).[5] EPR spectra of

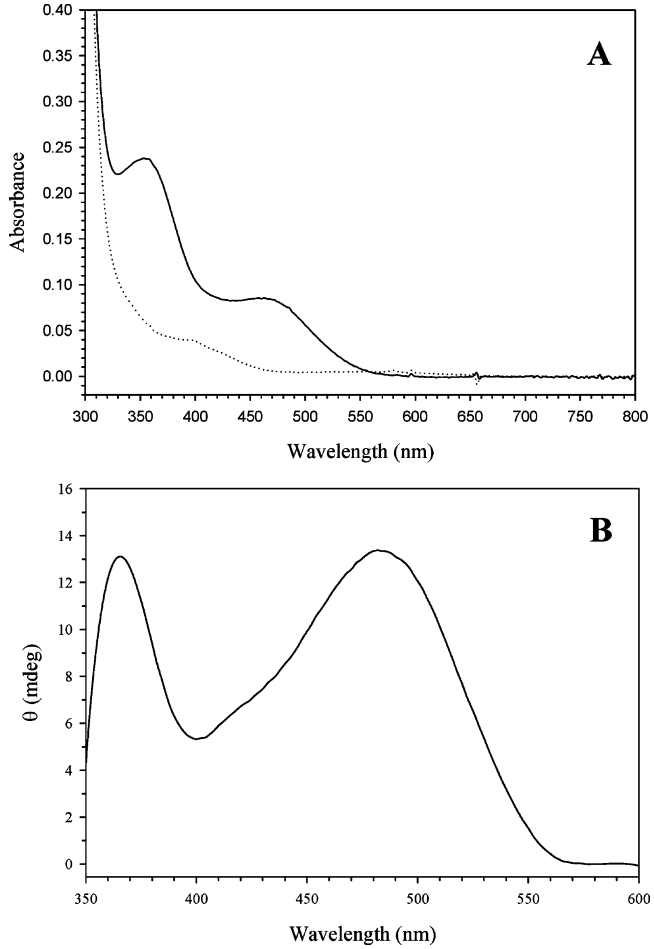

Figure 2. UV−visible and CD spectra of *A. thaliana* SO. (A) UV−visible spectrum of oxidized (solid line) and sulfite-reduced (dashed line) enzyme. The 360 and 480 nm absorption bands (oxidized enzyme) are attributed to a combination of enedithiolate-to-molybdenum and cysteine-to-molybdenum charge-transfer bands. (B) Circular dichroism spectrum of oxidized enzyme.

the low-pH, high-pH, and phosphate-complexed forms of SO from either bovine or chicken enzymes have been reported.[5,11a,32,33] The EPR spectra of the low- (lpH) and high-pH (hpH) forms of SO have been obtained and, as seen in Figure 3, exhibit considerably better resolution than previously reported (the lpH form, in particular, appeared to be a mixture of forms).[18] It can be seen that the spectral features are indeed quite comparable to those seen for other sulfite oxidases. The hyperfine splitting due to a solvent-exchangeable proton seen in the lpH spectra of bovine and chicken enzyme is not readily observed in *A. thaliana* SO, although the broad shoulder observed at $g = 2$ in the lpH form of SO was slightly sharpened upon exchange of the protein into deuterated buffer. Addition of sodium chloride to the lpH sample buffer resulted in a slightly more intense low-field signal suggestive of unresolved proton hyperfine splitting. The estimated *g*-value for the midpoint of the lpH NaCl low-field feature ($g_1 = 2.0033$) correlates well with that seen for chicken SO ($g_1 = 2.0037$, $A(^1H)_1 = 0.85$ mT). Interestingly, the *g*-values seen for the lpH form of SO are comparable to the *g*-values observed for the chicken lpH D_2O sample by Dhawan et. al.[7] As reported previously,[18] we are unable to observe the phosphate-inhibited signal that has been seen with the chicken protein (signal appeared as the lpH form in up to 0.1 M NaH_2PO_4). Table 1 lists the *g*-values obtained for the various forms

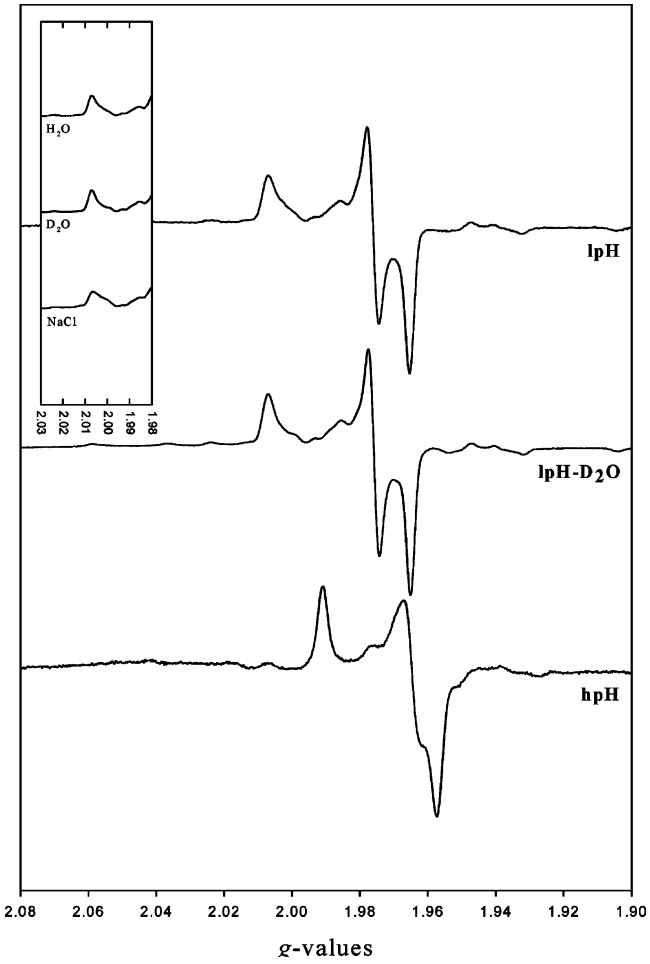

Figure 3. EPR spectra of *A. thaliana* SO. EPR spectra were recorded on SO (100−200 μM) reduced with excess sulfite (4 mM) and reoxidized with one-half equivalent of potassium ferricyanide. Buffers were 50 mM bis-Tris-propane, pH 6.0 (lpH), 50 mM bis-Tris-propane, pH 6.0, 100 mM NaCl (lpH NaCl, full spectrum not shown), 50 mM bis-Tris-propane, pD 6.0 (lpH D_2O), and 50 mM glycine, pH 10.0 (hpH). Instrument settings were 9.46 GHz microwave frequency, 2 mW microwave power, 100 kHz modulation frequency, 5.0 G modulation amplitude. Sample temperature was 150 K. Inset shows the expanded $g = 2$ region for the three lpH samples.

Table 1. EPR Data for *A. thaliana* SO and Avian SO

source	signal	1	2	3	av.	ref
A. thaliana	lpH	2.0070	1.9760	1.9654	1.9828	present work
	lpH D_2O	2.0072	1.9760	1.9652	1.9828	present work
	lpH NaCl	2.0065	1.9757	1.9654	1.9825	present work
	hpH	1.9909	1.9645	1.9574	1.9709	present work
chicken	lpH	2.0037	1.9720	1.9658	1.9805	5
	hpH	1.9872	1.9641	1.9531	1.9681	5
	lpH D_2O	2.007	1.974	1.968	1.983	7

of SO and compares these with the corresponding parameters for the chicken enzyme.

Resonance Raman Studies. Resonance Raman spectra have been obtained for redox-cycled *A. thaliana* SO prepared in both $H_2{}^{16}O$ and $H_2{}^{18}O$ buffer (Figure 4), the data being collected using 488 nm (20 490 cm^{-1}) excitation in resonance with a LMCT band at 480 nm (20 830 cm^{-1}). The spectrum of the sample prepared in $H_2{}^{16}O$ exhibits three intense features in the 840−940 cm^{-1} region at 896, 877, and 864 cm^{-1}, where symmetric (ν_s) and antisymmetric (ν_{as}) Mo−O_{oxo} stretching modes are anticipated to occur. The 896 cm^{-1} mode is

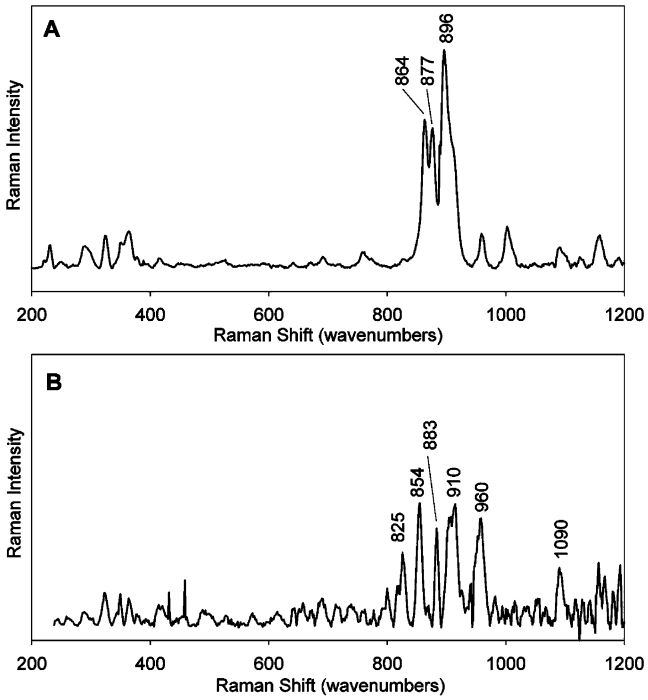

Figure 4. Resonance Raman spectra of oxidized *A. thaliana* SO redox-cycled in (A) $H_2{}^{16}O$ and (B) $H_2{}^{18}O$. Both spectra were collected at 30 K using 488 nm excitation.

approximately twice as intense as the lower frequency 877 and 864 cm^{-1} modes. These vibrational frequencies are similar to those previously observed for wild-type recombinant human SO: ν_s(Mo−O_{oxo}) at 903 cm^{-1} and ν_{as}(Mo═O) at 881 cm^{-1},[14] and in dioxomolybdenum(VI) model compound studies: ν_s-(Mo−O_{oxo}) from 858 to 938 cm^{-1}, and ν_{as}(Mo−O_{oxo}) from 835 to 898 cm^{-1}.[34] Enzyme samples were redox-cycled in $H_2{}^{18}O$, and the resultant resonance Raman spectrum shows vibrations in the M−O_{oxo} stretching region at 883, 854, and 825 cm^{-1}. Features at ∼910, ∼960, and 1090 cm^{-1}, observed in the spectrum of labeled enzyme, are also observed in the natural abundance data set, with the 910 cm^{-1} band being present as a high frequency shoulder on the intense 896 cm^{-1} band. As such, it is evident that the signal-to-noise ratio for the ^{18}O data set is markedly poorer than the natural abundance data set, and this effect was consistently observed over multiple runs with several independently prepared samples. Nevertheless, the features observed at 883, 854, and 825 cm^{-1} appear to be unique to ^{18}O-labeled enzyme. The enedithiolate-to-molybdenum and cysteine-to-molybdenum charge-transfer bands at 360 and 480 nm, respectively, are very sensitive to changes in molybdenum coordination as exemplified by the UV/vis spectra of the C207S and R160Q mutants of recombinant human SO. The C207S mutation resulted in a trioxomolybdenum species with complete loss of absorbance at 480 nm.[14,49] The R160Q mutant enzyme displayed a blue shift of approximately 25 nm in the 480 nm band and a significant decrease in the intensity of the 350 nm band.[50] The UV/vis spectrum for the ^{18}O-labeled enzyme in this

(48) The active sites of chicken SO and plant SO are nearly identical. Either structure could have been used as a starting point for the theoretical work, but the theoretical models were being examined prior to publication of the plant enzyme crystal structure.

(49) George, G. N.; Garrett, R. M.; Prince, R. C.; Rajagopalan, K. V. *J. Am. Chem. Soc.* **1996**, *118*, 8588−8592.
(50) Garrett, R. M.; Johnson, J. L.; Graf, T. N.; Feigenbaum, A.; Rajagopalan, K. V. *Proc. Natl. Acad. Sci. U.S.A.* **1998**, *95*, 6394−6398.

study is identical to that shown for unlabeled, oxidized enzyme (data not shown), indicating that the molybdenum center is intact. Samples were also prepared in which oxidized enzyme was exchanged into $H_2{}^{18}O$ buffer and incubated for 36 h prior to recording the rR spectrum. The same treatment was performed on a sample reduced with sulfite after exchange into $H_2{}^{18}O$ buffer. For the oxidized sample, no incorporation of label was evident in the rR spectrum, and for the reduced sample, the rR spectrum obtained was identical to that of Figure 4B (data not shown).

Density Functional Calculations. Electronic structure and vibrational frequency calculations were performed on geometry optimized computational models of the dioxomolybdenum center of oxidized SO. For both of these models, frequency calculations were performed at two geometries. The first was an unconstrained geometry (referred to as "unconstrained" in the text) and on a geometry in which the $O_{ax}-Mo-S-C$ dihedral angle was constrained at 90° (referred to as "90°-fixed" throughout). The starting geometry for the large and small models was taken directly from the crystal structure of chicken liver SO reported by Kisker et al. (PDB accession code of 1SOX).[16,48] The 2-carbophosphate group of the dihydropyran ring was replaced with a vinyl group, and the pyrazine portion of the pterin ring was protonated in the large model. The small model utilized 1,2-dimethyl dithiolene and methyl thiolate to model the pyranopterin−dithiolene and cysteine sulfur ligands, respectively.

Electron density isosurfaces for the unoccupied redox-active molecular orbital in dioxo, $[MoO_2(S_2C_2Me_2)(SCH_3)]^-$, and the large model, $[LMoO_2(SCH_3)]^-$, are depicted in Figure 5 for the 90°-fixed geometries. These isosurfaces show that the two terminal oxo ligands are highly *inequivalent* electronically. The nature of this redox-active molecular orbital is of key mechanistic importance, as it is the putative electron acceptor orbital in the oxygen atom transfer reaction with sulfite. This orbital is principally comprised of a very strong d−p π antibonding interaction between the Mo d_{xy} orbital and an O_{eq} p orbital. For unconstrained $[MoO_2(S_2C_2Me_2)(SCH_3)]^-$, the redox-active molecular orbital is comprised of 52% Mo d_{xy}, 17.3% O_{eq} p, and 3.2% O_{ax} p atomic orbital character. For the 90°-fixed calculations, the relevant atomic orbital contributions are 52% Mo d_{xy}, 25.2% O_{eq} p, and a mere 0.6% for the O_{axial} p orbital. It appears from the calculations on $[MoO_2(S_2C_2Me_2)(SCH_3)]^-$ and $[LMoO_2(SCH_3)]^-$ that the nature of the redox-active molecular orbital is not a function of the $O_{ax}-Mo-S_{Cys}-C$ dihedral angle, in agreement with earlier studies, and possesses little O_{ax} character.[35]

Calculated frequencies and mode assignments for the unconstrained and 90°-fixed model geometries are provided in Tables 2 and 3 for the large and small models, respectively. Calculations were performed on a natural abundance $^{16}O_{eq}/^{16}O_{ax}$ model in addition to the $^{18}O_{eq}/^{16}O_{ax}$, $^{16}O_{eq}/^{18}O_{ax}$, $^{18}O_{eq}/^{18}O_{ax}$, isotopomers. A pictorial description of the three key normal modes that possess appreciable $M-O_{oxo}$ stretching character is shown in Figures 6 and 7 for the large and small models in the 90°-fixed geometry, respectively. Results for the $^{16}O_{eq}/^{16}O_{ax}$ and $^{18}O_{eq}/^{18}O_{ax}$ isotopomers indicate that both possess vibrational modes described as symmetric (ν_s) and antisymmetric (ν_{as}) $Mo-O_{oxo}$ stretches, albeit with noticeable mode localization resulting from the low symmetry molecular environment. For the $^{16}O_{eq}/^{16}O_{ax}$ isotopomer, the large model calculation shows that ν_{as} mixes with a pyranopterin−dithiolene mode that possesses C−O pyran and C−S dithiolene stretching character. A similar modal structure is observed for the small model, except that the C−S stretch of the dithiolene possesses substantial $Mo-O_{eq}$ character. The pyranopterin−dithiolene-based vibration does not appreciably mix with either ν_s or ν_{as} in the $^{18}O_{eq}/^{18}O_{ax}$ isotopomer as a result of the greater frequency difference between the $Mo-O_{oxo}$ stretches and $\nu_{C-O/C-S}$. Furthermore, ν_s and ν_{as} are shifted 48 and ~43 cm^{-1} lower in frequency, respectively, compared to that calculated for the natural abundance models. This is in good agreement with the ~48 cm^{-1} shift predicted for the reduced mass of a diatomic 970 cm^{-1} $Mo-O_{oxo}$ oscillator. Vibrational calculations performed on both model systems indicate that ^{18}O-labeling of a single oxo ligand significantly decouples and localizes the two Mo=O stretching modes (i.e., ν_s and ν_{as} now become ν_{ax} and ν_{eq}). Most notably, the $Mo-O_{oxo}$ unit labeled with ^{18}O is shifted to lower vibrational frequency. The large model calculation for the $^{18}O_{eq}/^{16}O_{ax}$

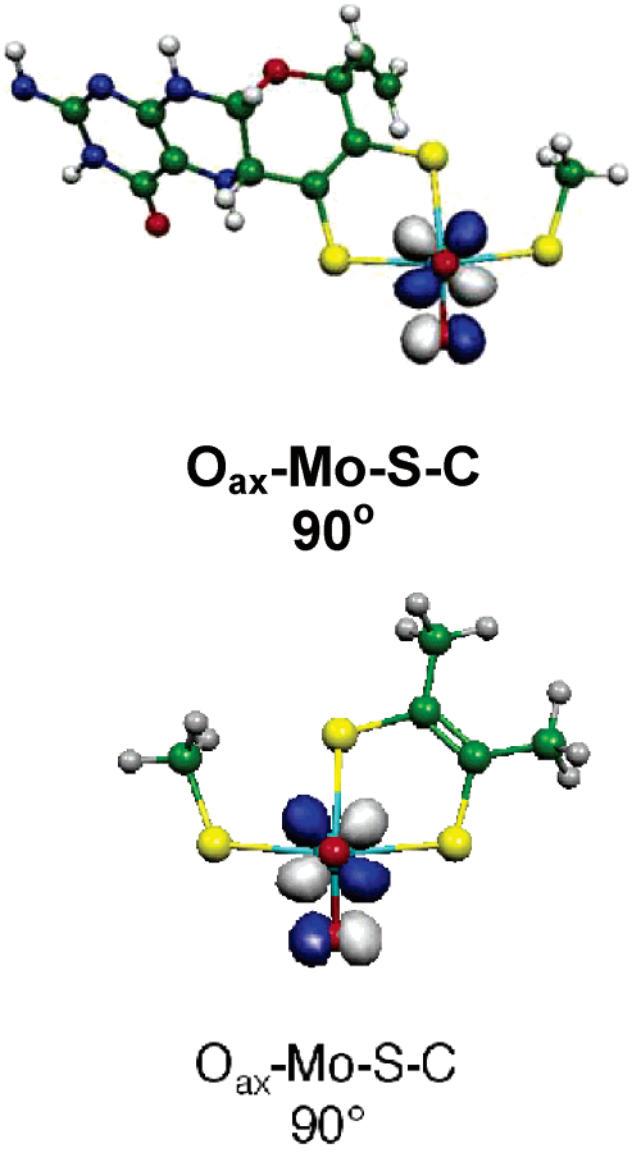

Figure 5. Molecular orbital isosurfaces of the LUMOs of the 90°-fixed optimized geometries of the (*top*) large model and (*bottom*) small model of the dioxo-Mo(VI) centers used in this study.

Table 2. Calculated Vibrational Frequencies and Assignments for Each Isotopomer of the Large Model in Both the 90°-Fixed and Unconstrained Geometries[a]

Natural Abundance		
90°-fixed	unconstrained	assignment
978	975	ν_s(Mo═O)
966	962	ν_{as}(Mo═O) − ν[(C−S)pterin/(C−O)pyran]
952	959	ν_{as}(Mo═O) + ν[(C−S)pterin/(C−O)pyran]
$^{16}O_{axial}/^{18}O_{equatorial}$		
90°-fixed	unconstrained	assignment
975	968	ν(Mo═O), axial
965	961	ν [(C−S)pterin/(C−O)pyran]
910	920	ν(Mo═O), equatorial
$^{18}O_{axial}/^{16}O_{equatorial}$		
90°-fixed	unconstrained	assignment
967	969	ν_s(Mo═O), mostly Mo═O(eq) − ν[(C−S)pterin/(C−O)pyran]
958	960	ν_s(Mo═O), mostly Mo═O(eq) + ν[(C−S)pterin/(C−O)pyran]
925	920	ν_{as}(Mo═O), mostly Mo═O(axial)
$^{18}O_{axial}/^{18}O_{equatorial}$		
90°-fixed	unconstrained	assignment
965	961	ν[(C−S)pterin/(C−O)pyran]
930	926	ν_s(Mo═O)
908	916	ν_{as}(Mo═O)

[a] All frequencies are in cm^{-1} with no scaling.

Table 3. Calculated Vibrational Frequencies and Assignments for Each Isotopomer of the Small Model in Both the 90°-Fixed and Unconstrained Geometries[a]

Natural Abundance			
90°-fixed	assignment	unconstrained	assignment
962	ν_s(Mo═O)	957	ν_s(Mo═O)
947	νMo═O_{eq} − ν(C−S)	947	ν_{as}(Mo═O) − ν(C−S)
936	νMo═O_{eq} + ν(C−S)	941	ν_{as}(Mo═O) + ν(C−S)
$^{16}O_{axial}/^{18}O_{equatorial}$			
90°-fixed	assignment	unconstrained	assignment
958	νMo═O_{ax} + ν(C−S)	955	νMo═O_{ax} + ν(C−S)
945	νMo═O_{ax} − ν(C−S)	945	ν(C−S)
896	νMo═O_{eq} + ν(C−S)	906	νMo═O_{eq} + ν(C−S)
$^{18}O_{axial}/^{16}O_{equatorial}$			
90°-fixed	assignment	unconstrained	assignment
947	νMo═O_{eq} − ν(C−S)	952	νMo═O_{eq} − ν(C−S)
943	νMo═O_{eq} + ν(C−S)	946	ν(C−S)
911	νMo═O_{ax} − ν(C−S)	907	νMo═O_{ax} − ν(C−S)
$^{18}O_{axial}/^{18}O_{equatorial}$			
90°-fixed	unconstrained	assignment	
947	946	ν(C−S)	
914	910	ν_s(Mo═O)	
895	903	ν_{as}(Mo═O)	

[a] All frequencies are in cm^{-1} with no scaling.

isotopomer yields distinct ν_{ax} and ν_{eq} modes, while Mo−O_{ax} vibrational character is mixed into the dithiolene C−S stretch, ν_{C-S}, in the small molecule calculation. The large model calculation for the $^{16}O_{eq}/^{18}O_{ax}$ isotopomer also yields relatively distinct ν_{ax} and ν_{eq} modes, with the Mo−O_{eq} vibration mixing with the C−O pyran/C−S dithiolene stretch. In the small molecule calculation, the $^{16}O_{eq}/^{18}O_{ax}$ isotopomer possesses distinct ν_{ax} and ν_{eq} modes, with noticeable ν_{eq}/ν_{C-S} mode mixing and some Mo−O_{eq} character mixed in all three modes. In summary, the low symmetry of the oxidized [(dt)MoO_2(SR)]$^{1-}$ dioxo site results in some Mo−O_{oxo} mode localization which becomes more pronounced in the $^{18}O_{eq}/^{16}O_{ax}$ and $^{16}O_{eq}/^{18}O_{ax}$ isotopomers. Therefore, for this system, vibrational frequency shifts upon ^{18}O substitution are generally consistent with those expected from the reduced mass of a diatomic Mo−O_{oxo} oscillator.

Analysis

Bonding Calculations and Nature of the Excited-State Distortion. The two oxo ligands in small molecule dioxo $[MoO_2]^{2+}$ sites are often related by either a C_2 or C_s symmetry operation. This results in well-defined ν_s and ν_{as} normal modes. As the lowest unoccupied molecular orbital (LUMO), or redox-active orbital, is delocalized over both oxo ligands in the C_2/C_s case, excited-state distortions occur along both oxo ligands, resulting in Albrecht A-term enhancement of only the symmetric ν_s vibration.[39] Experimentally, ν_s is observed to be considerably more intense than ν_{as} in the resonance Raman spectra of symmetric $[MoO_2]^{2+}$ sites.[40] The electron density isosurfaces for the redox-active molecular orbital in both the large and small models of SO_{ox} clearly show that the two terminal oxo ligands are highly inequivalent electronically, and the redox orbital possesses strongly antibonding interactions between the Mo d_{xy} orbital and the O_{eq} p orbital. Thus, ligand-to-metal charge transfer (LMCT) transitions, described as one-electron promotions from filled molecular orbitals with appreciable $S_{dithiolene}$ and/or S_{Cys} character to the empty redox orbital, should result in a marked excited-state distortion along the Mo−O_{eq} bond, with no distortion along Mo−O_{ax}. Therefore, any vibrational mode possessing appreciable Mo−O_{eq} stretching character should be resonantly enhanced in the Raman spectrum of SO. Thus, for the $^{16}O_{eq}/^{16}O_{ax}$ and $^{18}O_{eq}/^{18}O_{ax}$ isotopomers, both ν_s and ν_{as} will be resonantly enhanced, as a Mo−O_{eq} displacement is observed in both of these normal modes. As such, the excited-state distortion can be thought of as a linear combination of the ν_s and ν_{as} normal modes (Figure 8). Furthermore, to the extent

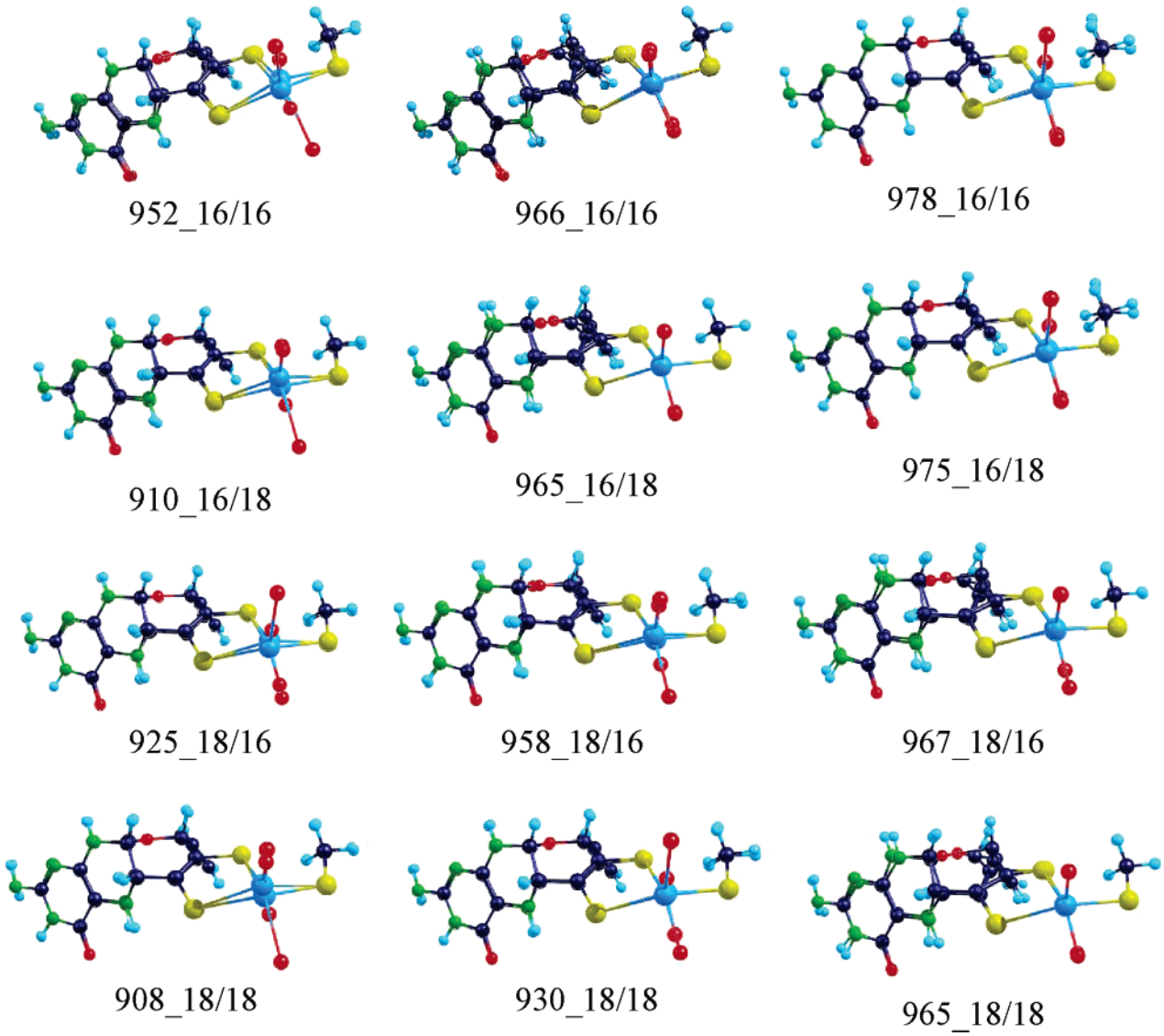

Figure 6. Pictorial description of the three key normal modes that possess appreciable M−O_{oxo} stretching character for each isotopomer of the large model in the 90°-fixed geometry. All vibrational frequencies are in cm^{-1}, and the oxygen isotope ordering is $O_{axial}/O_{equatorial}$ arranged in rows. Images of the extrema of each normal mode were created using either Molekel 4.0[43] or ChemCraft V1.4[44].

that the C−O pyran/C−S dithiolene stretch is coupled to either ν_s or ν_{as}, this mode is anticipated to be resonantly enhanced as well.

Given the crystal structures of both (reduced) chicken and (oxidized) *A. thaliana* SO,[16,36] the most likely location for isotopic labeling of the terminal oxo ligands is at O_{eq}, as this ligand points directly toward the substrate/solvent access channel. For the $^{18}O_{eq}/^{16}O_{ax}$ isotopomer, the Mo−oxo vibrational modes are highly localized, and only ν_{eq} is anticipated to be resonantly enhanced when pumping into low-energy LMCT transitions. Although Mo−O_{eq} stretching character is observed in all three calculated modes for the $^{16}O_{eq}/^{18}O_{ax}$ isotopomer, and some resonance enhancement may be expected for all three of these vibrational modes, incorporation of a *single* ^{18}O label at O_{ax} is highly unlikely (vide supra). As such, the $^{16}O_{eq}/^{18}O_{ax}$ isotopomer will not be considered further.

Vibrational Assignments. The results of small molecule studies on dioxomolybdenum compounds are consistent in the fact that ν_s occurs at higher frequency than ν_{as}, and the $\nu_s - \nu_{as}$ frequency difference is ~30 cm^{-1}.[40] Assuming a simple O_{oxo}−Mo−O_{oxo} triatomic, the $\nu_{as}^{18}/\nu_{as}^{16}$ ratio is a function of the O_{oxo}−Mo−O_{oxo} bond angle according to

$$\left(\frac{\nu_{as}^{18}}{\nu_{as}^{16}}\right)^2 = \frac{m_O(m_{Mo} + 2m_O^{18}\sin^2\theta)}{m_O^{18}(m_{Mo} + 2m_O\sin^2\theta)}$$

where θ is half the O_{oxo}−Mo−O_{oxo} bond angle, and the m_i are the masses of either molybdenum or oxygen.[41] When the O_{oxo}−Mo−O_{oxo} bond angle is ~112°, the $\nu_{as}^{18}/\nu_{as}^{16}$ ratio is calculated to be 0.91. Similar relationships can be derived for the ν_s^{18}/ν_s^{16} ratio, and both expressions are consistent with experimental data which show that the $\nu_{as}^{18}/\nu_{as}^{16}$ and ν_s^{18}/ν_s^{16} ratios are 0.95.[40] Thus, previous vibrational studies on small molecule $[MoO_2]^{2+}$ sites, coupled with the vibrational modes determined for computational models of the *A. thaliana* SO active site, can now be used to make vibrational assignments for the natural abundance and ^{18}O-substituted dioxo active site.

The highest frequency mode observed in the $^{16}O_{eq}/^{16}O_{ax}$ natural abundance spectrum is found at 896 cm^{-1}. Although

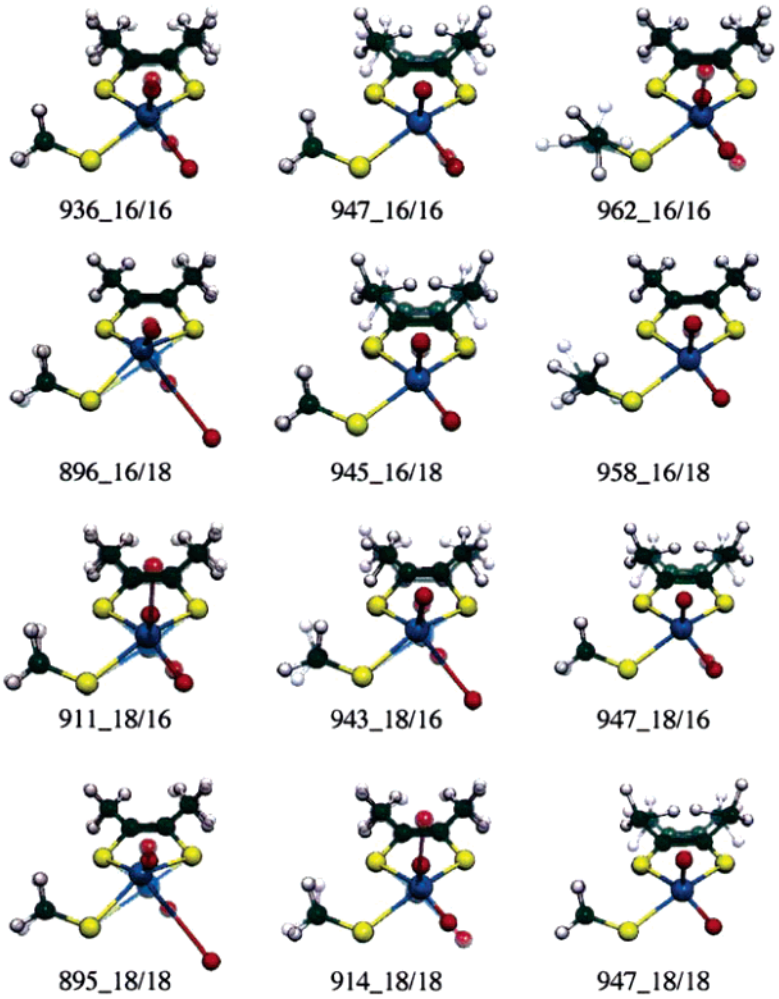

Figure 7. Pictorial description of the three key normal modes that possess appreciable M−O_{oxo} stretching character for each isotopomer of the small model in the 90°-fixed geometry. All vibrational frequencies are in cm^{-1}, and the oxygen isotope ordering is $O_{axial}/O_{equatorial}$ arranged in rows. Images of the extrema of each normal mode were created using either Molekel 4.0[43] or ChemCraft V1.4[44].

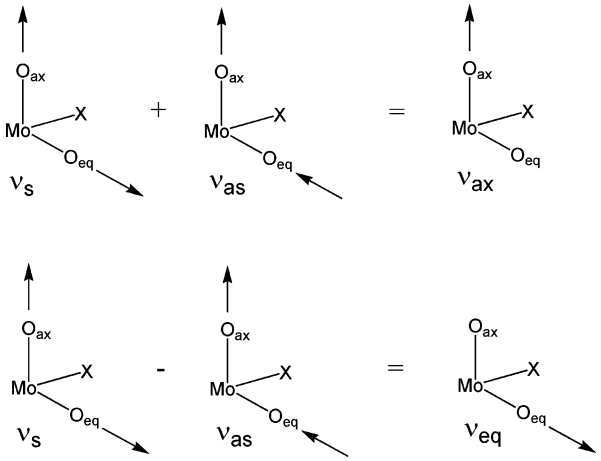

Figure 8. Symmetry coordinates for the *cis*-dioxo vibrations. Linear combinations of the symmetric (ν_s) and antisymmetric (ν_{as}) *cis*-MoO_2 modes yield the localized modes ν_{ax} and ν_{eq}. The localized modes describe Mo═O vibrations along the Mo−O_{ax} (ν_{ax}) and Mo−O_{eq} (ν_{eq}) bonds. Excited-state distortions which only occur along the Mo−O_{eq} result in resonance Raman enhancement of both ν_s and ν_{as} in the normal mode approximation (see text).

approximately 7% lower in frequency than the DFT calculated ν_s, this frequency is in good agreement with the frequency of ν_s determined for small molecule $[MoO_2]^{2+}$ sites.[40] As such, we assign the $^{16}O_{eq}/^{16}O_{ax}$ 896 cm^{-1} mode as ν_s. Since the experimentally observed $\nu_s - \nu_{as}$ frequency difference in small molecule $[MoO_2]^{2+}$ sites is ~30 cm^{-1} and the DFT calculated $\nu_s - \nu_{as}$ frequency difference is 26 cm^{-1}, we assign the 864 cm^{-1} vibration in $^{16}O_{eq}/^{16}O_{ax}$ SO ($\nu_s - \nu_{as} = 32$ cm^{-1}) as ν_{as}. The 877 cm^{-1} vibration is therefore assigned as $\nu_{C-O/C-S}$, a vibrational mode of the pyranopterin−dithiolene that possesses both C−O pyran and C−S dithiolene stretching character. The relative resonance Raman enhancement ratio $I\nu_s/I\nu_{as}$, observed in Figure 4, is approximately 2:1, a marked reduction from the ratio observed in small molecules where both oxo ligands are related by a symmetry element.[40] This is important, as the markedly different intensity enhancement ratio provides direct experimental evidence for a redox orbital oriented in the equatorial plane that arises from an antibonding interaction between the Mo d_{xy} orbital and only the O_{eq} p orbital. This is in marked contrast to the symmetric $[MoO_2]^{2+}$ case where the redox-active molecular orbital is delocalized over *both* oxo ligands.

The analysis of the ^{18}O-labeled spectrum presents some difficulties, as there may be slow exchange (i.e., slower than the catalytic turnover rate) of the initially labeled $^{18}O_{eq}/^{16}O_{ax}$ enzyme to yield an $^{18}O_{eq}/^{18}O_{ax}$ site. Support for this assertion is derived from recent ESEEM results, which show incorporation

of ^{17}O label at both the axial and equatorial positions in the high-pH form of chicken SO.[47] A previous rR study on the Mo domain of recombinant human SO, redox-cycled in $H_2{}^{18}O$, reported that only one of the terminal oxo ligands incorporated label.[14] For the $^{18}O_{eq}/^{16}O_{ax}$ isotopomer, the nature of the excited-state distortion is along Mo−O_{eq} and only ν_{eq} should be resonantly enhanced within the localized mode approximation. The DFT results show that ν_{as} in the $^{16}O_{eq}/^{16}O_{ax}$ isotopomer is shifted ~41 cm^{-1} to yield ν_{eq} in the $^{18}O_{eq}/^{16}O_{ax}$ spectrum, in reasonable agreement with that predicted for an 896 cm^{-1} diatomic Mo−O_{oxo} oscillator (~44 cm^{-1}). As such, the 825 cm^{-1} mode in ^{18}O-labeled enzyme may be assigned as ν_{eq} ($\nu_{as} - \nu_{eq} = 39$ cm^{-1}), provided only O_{eq} is isotopically labeled. Under the assumption of a ν_s and ν_{as} normal mode approximation, which is not supported by the results of our DFT calculations, the predicted vibrational frequency shifts for the $^{18}O_{eq}/^{16}O_{ax}$ isotopomer are anticipated to be ~22 cm^{-1} for ν_s and ν_{as} when the functional form of these modes are given by

$$\nu_{as}^{s} = \frac{1}{\sqrt{2}}(\nu_{ax} \pm \nu_{eq})$$

In fact, the relationship between the frequency shift of the two oxo modes associated with the $[MoO_2]^{2+}$ unit and the vibrational mode description is that the total sum frequency shift of the two oxo stretches is ~44 cm^{-1}, with all of this attributed to one vibration in the local mode approximation, and ~22 cm^{-1} for each vibration in the normal mode picture. Provided the local, ν_{ax} and ν_{eq}, mode approximation is not applicable for the $^{18}O_{eq}/^{16}O_{ax}$ isotopomer, an alternative assignment finds ν_s at 883 cm^{-1} and ν_{as} at 854 cm^{-1}. Here the total sum frequency shift of the two oxo stretches is ~36 cm^{-1}, in reasonable agreement with the predicted ~44 cm^{-1} shift.

For the case where both terminal oxo ligands become labeled due to slow exchange between O_{eq} and O_{ax} sites, a vibrational mode description with ν_s and ν_{as} normal modes is applicable. Since both the $\nu_{as}^{18}/\nu_{as}^{16}$ and ν_s^{18}/ν_s^{16} frequency ratios are experimentally determined to be 0.95 in small molecule $[MoO_2]^{2+}$ sites, similar to the results of our DFT calculations, the 854 cm^{-1} vibration is assigned as ν_s ($0.95 \times 896 = 851$) and the 825 cm^{-1} vibration is assigned as ν_{as} ($0.95 \times 864 = 821$). The $\nu_{C-O/C-S}$ vibrational mode is not anticipated to be resonantly enhanced, as the calculations show that it does not effectively couple with ν_s and ν_{as} due to the poor energy match. However, a band is observed at 883 cm^{-1} in the ^{18}O-labeled sample and may be tentatively assigned as the $\nu_{C-O/C-S}$ mode. Interestingly, the $I\nu_s/I\nu_{as}$ resonance enhancement ratio for this $^{18}O_{eq}/^{18}O_{ax}$ assignment is approximately 2:1, the same as in the $^{16}O_{eq}/^{16}O_{ax}$ spectrum and consistent with a redox-active molecular orbital that is Mo d_{xy}−O_{eq} p antibonding in nature.

Discussion

Here we discuss the further kinetic and spectroscopic characterization of the SO from *Arabidopsis thaliana*. The pH dependence of the steady-state kinetics of SO is similar to that seen previously with the chicken enzyme, and the previously reported $K_m^{sulfite}$ value is comparable.[25] However, rapid kinetic experiments following the reduction of SO by sulfite demonstrated that the kinetic rate of substrate oxidation is much faster in the plant enzyme. Even at 5 °C, substrate oxidation was complete within the dead-time of the stopped-flow apparatus, indicating that k_{red} for the plant enzyme is at least 10 times greater than that for the enzyme from chicken liver. Neither rat outer-mitochondrial membrane cytochrome b_5 nor horse heart cytochrome *c* are effective oxidizing substrates for SO, leaving open the question as to the physiological electron acceptor for the enzyme.

The EPR of SO at low and high pH exhibits Mo(V) signals with *g*-values very similar to those observed for vertebrate sulfite oxidases (see Table 1). Still, significant differences are apparent, which indicate unique aspects of the SO active site. We have been unable to detect a phosphate-complexed EPR signal under a variety of experimental conditions. In addition, the lpH signal, particularly the low-field region, does not exhibit the obvious proton hyperfine splitting seen in the lpH signal for chicken SO[32] (although our lpH samples did exhibit some narrowing of spectral features on exchange into D_2O, which suggests a small unresolved proton splitting). ESEEM experiments on chicken SO have suggested that the proton hyperfine splitting, seen in the lpH form but not in the hpH form, is due to a rotation about the Mo−OH bond, with strong coupling observed only when the proton lies in the equatorial plane of the molybdenum center, maximizing interaction with the d_{xy} redox orbital that possesses the unpaired electron.[11] In the hpH form, the Mo^V−OH bond is thought to have rotated out of plane due to an interaction with a hydroxide or water molecule, which results in the loss of the observed proton hyperfine splitting.

Our resonance Raman spectroscopic investigation on the oxidized active site of *A. thaliana* SO provides experimental support for the recently proposed Mo d_{xy}−O_{eq} π^* antibonding interaction in the SO_{ox} LUMO,[35] allowed for the assignment of a vibrational mode associated with the pyranopterin−dithiolene, and addressed issues regarding active-site oxygen trafficking under turnover conditions. Prominent Raman vibrations in the 800−1000 cm^{-1} region occur at 896, 864, and 877 cm^{-1} and have been assigned as ν_s, ν_{as}, and $\nu_{C-O/C-S}$, respectively. Furthermore, the relative intensities of ν_s and ν_{as} have been interpreted in terms of an excited-state distortion solely along the Mo−O_{eq} bond, indicating O_{ax} and O_{eq} are quite inequivalent electronically. Isotopic labeling of enzyme samples turned over in $H_2{}^{18}O$ is inconclusive regarding whether one or both of the terminal oxo ligands incorporate label. Provided O_{eq} is initially labeled under turnover conditions, labeling of O_{ax} would likely occur on a much longer time scale relative to catalysis, and this is therefore not likely to be of mechanistic significance. Previous Raman studies on recombinant human SO, prepared by tryptic cleavage of the K108R holoenzyme variant and overexpression of the His-tagged Mo domain, possessed vibrational bands at 903 and 881 cm^{-1}. These were assigned as ν_s and ν_{as}, respectively, and due to their isotopic shifts in samples redox-cycled in $H_2{}^{18}O$, it was suggested that only one of the terminal oxo ligands was exchanged.[14] Given the necessary loss of symmetry of the center associated with labeling at only one of the two Mo═O groups, however, it is to be emphasized that the assignment of symmetric and asymmetric modes is not in fact appropriate, and the system is best treated as having localized axial and equatorial Mo═O modes rather than delocalized symmetric and antisymmetric modes.

The X-ray structures of the (reduced) chicken enzyme[16] and the (oxidized) plant enzyme[36] reveal that O_{eq} is oriented directly into the solvent access channel and toward the substrate binding

site and, undoubtedly, represents the catalytically labile oxo ligand that is transferred to sulfite in the course of substrate oxidation. In addition to these obvious structural considerations, which strongly indicate that the O_{eq} is specifically transferred to sulfite in the course of oxygen atom transfer, various ideas have been suggested regarding how a specific oxo ligand is activated for catalysis in SO. The first may be considered to arise from breaking of the dioxomolybdenum symmetry by the ligand field and is supported by spectroscopic and computational studies on the small molecule analogue, $[(L\text{-}N_3)Mo^{VI}O_2(SCH_2Ph)]$.[42] In this case, the degeneracy of the two Mo=O π^* acceptor orbitals is lifted by torsional rotations about the $O-Mo-S_{thiolate}-C$ dihedral angle. This results in one Mo=O π^* acceptor orbital being lowered in energy, with the corresponding Mo=O bond being activated with respect to oxo atom transfer to substrate. Small molecule reactivity studies indicate that the activation of a specific oxo ligand for transfer to substrate is driven by the initial interaction of substrate with an active-site oxo ligand, providing a pretransition state contribution to the activation energy. However, the active-site geometry of the oxidized enzyme is of very low symmetry, and the two oxo groups are thus quite inequivalent, electronically as well as structurally. Since O_{ax} does not possess a trans ligand whereas O_{eq} is oriented trans to a dithiolene sulfur donor, the $Mo-O_{eq}$ bond is likely the weaker of the two $Mo-O_{oxo}$ bonds. Thus, a key role for the dithiolene in the reductive half-reaction may be to promote oxygen atom transfer reactivity via a trans effect within the molybdenum coordination sphere.

The nature of the calculated LUMO for both the large, $[(dt)MoO_2(SCH_3)]^-$, and small, $[MoO_2(S_2C_2Me_2)(SCH_3)]^-$, models for SO_{ox} clearly shows the electronic asymmetry of the two oxo ligands. The bonding calculations show that the LUMO ($Mo-O_{eq}$ π^*) is highly stabilized ($\sim$1 eV) relative to the LUMO+1, which has $Mo-O_{ax}$ π^* character, indicating that the $Mo-O_{eq}$ π^* LUMO represents the acceptor orbital for electron density in the course of oxygen atom transfer reactivity with substrate.[35] The electron density isosurface plots in Figure 5 show that the LUMO is d−p π^* antibonding between the Mo d_{xy} orbital and one of the O_{eq} p orbitals, with O_{eq} contributing $\sim$20% total atomic orbital character to this MO. In contrast, the p orbitals of the O_{ax} oxygen do not contribute appreciably to the LUMO. Thus, the intrinsic asymmetry of the SO_{ox} site determines the precise nature of the LUMO and plays a defining role in the selection and activation of the equatorial Mo=O group in catalysis.

This bonding picture is supported by the experimentally determined relative resonance Raman enhancement ratio, $I\nu_s/I\nu_{as}$, in Figure 1 which is markedly reduced from that observed in many small molecules, where the two oxo ligands are symmetry-related. One-electron promotions from filled dithiolene and/or cysteine sulfur based MOs to the $Mo-O_{eq}$ π^* LUMO result in an excited-state distortion only along the $Mo-O_{eq}$ bond. That resonance enhancement of the oxo modes dominate the Raman spectrum of plant SO is most likely due to the fact that the acceptor orbital (LUMO or redox orbital) in SO_{ox} is strongly $Mo-O_{eq}$ antibonding with little dithiolene or cysteinyl character. As such, there is little change in Mo−S bonding between the ground and LMCT state, and no appreciable distortion occurs along these Mo−S modes, resulting in poor resonance enhancement. Since the displacement of the $Mo-O_{eq}$ bond in the excited state is along a coordinate described by a linear combination of the displacements encountered in the ν_s and ν_{as} vibrations (Figure 8), both ν_s and ν_{as} are observed to be appreciably resonantly enhanced. The resonance Raman enhancement intensity ratios for SO_{ox} are much lower than is seen with the more symmetric models, reflecting the extent to which the LUMO is localized on $Mo=O_{eq}$. Resonance Raman enhancement intensity ratios thus provide a sensitive probe of the character of the redox-active LUMO in SO_{ox} and are consistent with the results of our bonding calculations, indicating that the LUMO is Mo $d_{xy}-O_{eq}$ antibonding in nature. The large energetic stabilization of the SO_{ox} LUMO, coupled with good overlap between the substrate (sulfite) HOMO and the O_{eq} p orbital of the LUMO, allows for facile substrate attack at the equatorial oxo position. This translates to a reduction in the activation energy for catalytic oxygen atom transfer with concomitant increase in reaction rate, since occupation of the $Mo-O_{eq}$ d−p π^* orbital by the sulfite lone pair weakens the $Mo-O_{eq}$ bond, facilitates $Mo-O_{eq}$ bond cleavage, and promotes product release.

Acknowledgment. We thank Dr. M. Rivera (Department of Chemistry, University of Kansas) for the rat outer-mitochondrial membrane cytochrome b_5 expression construct. We also thank Erik Riebeseel for his participation in early portions of this work. This work was supported by a grant from the National Institutes of Health (GM-057378) to M.L.K. and (GM-59953) to R.H.

Supporting Information Available: Full author list for the Gaussian programs from ref 19 of text. This material is available free of charge via the Internet at http://pubs.acs.org.

JA0530873